

Reynolds stress and the physics of turbulent momentum transport

By PETER S. BERNARD¹ AND ROBERT A. HANDLER²

¹Department of Mechanical Engineering, University of Maryland, College Park, MD 20742, USA

²Laboratory for Computational Physics and Fluid Dynamics, Naval Research Laboratory, Washington, DC 20375, USA

(Received 20 September 1989 and in revised form 3 April 1990)

The nature of the momentum transport processes responsible for the Reynolds shear stress is investigated using several ensembles of fluid particle paths obtained from a direct numerical simulation of turbulent channel flow. It is found that the Reynolds stress can be viewed as arising from two fundamentally different mechanisms. The more significant entails transport in the manner described by Prandtl in which momentum is carried unchanged from one point to another by the random displacement of fluid particles. One-point models, such as the gradient law are found to be inherently unsuitable for representing this process. However, a potentially useful non-local approximation to displacement transport, depending on the global distribution of the mean velocity gradient, may be developed as a natural consequence of its definition. A second important transport mechanism involves fluid particles experiencing systematic accelerations and decelerations. Close to the wall this results in a reduction in Reynolds stress due to the slowing of sweep-type motions. Further away Reynolds stress is produced in spiralling motions, where particles accelerate or decelerate while changing direction. Both transport mechanisms appear to be closely associated with the dynamics of vortical structures in the wall region.

1. Introduction

A fundamental objective to which much research in turbulence is ultimately directed is to explain the nature of the transport process in turbulent shear flow culminating in the Reynolds stress. With such knowledge, the goal of developing a comprehensive closure scheme for use in prediction of turbulent flows may be significantly advanced. Perhaps the first comprehensive attempt at explaining the existence of Reynolds stress was given in Prandtl's (1925) mixing-length theory. In this, Prandtl proposed that Reynolds stress reflects the net transport of momentum across a plane arising from the random movement of fluid particles in the presence of a mean shear. In essence, eddies of fluid carry, unchanged, the average momentum of their original location to their destination a mixing length away. Since the mean velocity is non-constant, its difference between the initial and final locations of a particle correlates with the direction of travel, so that a momentum flux and consequently Reynolds stress is created. With the proviso that the mixing length should be relatively small, Prandtl used this physical model to justify the representation of Reynolds stress in the form of a gradient law.

For the purposes of the present work it is useful to make a distinction between the physical idea advanced by Prandtl regarding the physics of momentum transfer and

the deduction of a gradient transport law from it. Some elements of the former undoubtedly have considerable merit, while the later step is of questionable validity. For example, Corrsin (1974) effectively showed that the mixing length must ordinarily be of the same scale as that of significant variation in the mean velocity field. As a consequence, the assumption that the mixing length is small is not tenable except in unusual cases. The occurrence of such anomalous flows as a wall jet (Hinze 1975, p. 580) and transpired channel (Piomelli, Moin & Ferziger 1989) and the less than satisfactory performance of gradient closure schemes in the computation of complex flows (Lakshminarayana 1986) provide additional evidence to prove the inadequacy of the gradient model.

Since the work of Prandtl much effort has been expended in deriving methods for estimating the mixing length or eddy viscosity (Hinze 1975). Empirical and dimensional arguments have been applied in these developments which largely skirt direct consideration of physical mechanisms. Beyond the scope of Prandtl's theory, the primary focus in explaining Reynolds stress has relied less on consideration of fundamental physics than on the postulation of constitutive forms of the Reynolds stress tensor (Lumley 1983). These pursue the use of appropriate invariance principles to guide the development of formal mathematical constructions. In some theories (Speziale 1987) these go well beyond the framework of the gradient model. While such approaches bring into play a wealth of physical ideas of turbulent flow, these are often not directly involved with the mechanisms of momentum transport.

In recent times considerable attention has also been paid to exploring the phenomenological properties of coherent motions in the turbulent wall region (Wallace 1985; Robinson, Kline & Spalart 1988). In effect, any progress in this area should be of considerable importance towards explaining the physics of Reynolds stress, since burst and sweep events in turbulent boundary layers, which are a manifestation of the presence of vortical structures, are intrinsically associated with the turbulent transport of momentum. On the surface, such motions would appear to be one aspect of the kind of transport process described by Prandtl. However, if one is to obtain a practical recipe for the prediction of Reynolds stress from knowledge of such mechanisms, then much greater precision regarding the particulars of the coherency and how it relates to the instantaneous Reynolds stress is required. This is an area which current analyses of coherent structures have yet to treat in great depth.

In consideration of the large extent to which turbulent transport processes depend upon the dynamics of fluid particle motions, it may be expected that there is considerable benefit to taking the Lagrangian perspective in the analysis of Reynolds stress. This point of view was taken very early on by Taylor (1932) in a related study of vorticity transport. Over the years, several analyses of particle trajectories in shear flows have been made (Deardorff & Peskin 1970; Peskin 1974), though these have been limited by the technical difficulties of obtaining Lagrangian data. Recently, however, with the development of direct numerical simulations of turbulent flow as a practical tool, it has become possible to study the Lagrangian statistics of particle motions to any desired extent.

A recent study (Bernard, Ashmawey & Handler 1989*a, b*) has demonstrated the potential for explaining the physics of Reynolds stress which may be had from the analysis of particle paths in turbulent flow. The mechanisms for momentum transport were investigated at the point $y^+ = 15.8$ in the wall region of channel flow, by using ensembles of computed particle paths to evaluate a Lagrangian decomposition of the Reynolds stress into component physical processes. Some

limited results were also obtained further from the wall at $y^+ = 37.5$. It was found that the gradient mechanism overpredicts the Reynolds stress at $y^+ = 15.8$. In compensation, significant positive contributions to Reynolds stress came from non-gradient transport processes, reflecting the inadequacies of a local linear approximation to the mean velocity field, and the influence of pressure and viscous forces in changing the momentum of particles along their paths. To connect these results to the phenomenological aspects of boundary layers, the paths contributing most significantly to instantaneous Reynolds stress were visualized. Such paths, which were also implicated as the source of non-gradient transport, tended to be highly vortical with generally large displacements in the wall-normal direction.

The success of the Lagrangian technique in investigating momentum transport at primarily a single point has prompted interest in applying the technique throughout the wall region with the intent of developing a comprehensive description of the physics of momentum transport in the turbulent boundary layer. In particular, it is of interest to map out the relative trends of gradient and non-gradient effects across the wall layer and to find an explanation for these in terms of the particular motions of fluid particles. The insights provided by this analysis can be of considerable benefit in the construction of Reynolds stress models and in tying the presence of coherent structures to the formation of Reynolds stress.

The present study incorporates a greatly expanded data base of particle paths in pursuit of these objectives. Six ensembles of particle trajectories are obtained which have terminal points at six locations in the region encompassing $0 \leq y^+ \leq 40$, where $y^+ \equiv U_\tau y/\nu$, y is the distance from the wall, U_τ is the friction velocity, and ν is the kinematic viscosity. With the view afforded by this data a fairly complete picture of the origins of Reynolds stress in the wall region emerges. It is shown that it is most natural to consider the Reynolds stress as originating from two physical mechanisms encompassing the effects of displacement and acceleration of fluid particles. The former, which is the more significant of the two, corresponds to the process envisioned by Prandtl in which transport occurs through displacements of fluid particles without a change in momentum. A principal result of the study is to show that one-point models, such as the gradient transport law, are incapable of describing this process, so that it is inappropriate to view the Reynolds stress as arising from primarily a gradient mechanism supplemented by non-gradient corrections. Furthermore, it will be shown that the displacement transport process as a whole has a natural representation in terms of a global integral of the mean velocity gradient.

The second fundamental process affecting the Reynolds stress entails systematic accelerations and decelerations of fluid particles brought about by the influence of pressure and viscous forces. Close to the wall this involves the deceleration of sweep events resulting in a reduction of the total Reynolds stress. Further from the wall Reynolds stress is produced when fluid particles decelerate or accelerate while changing direction. These motions appear to be largely disjoint from those most responsible for displacement transport, though both sources of Reynolds stress may be manifestations of vortical structures containing a significant streamwise vorticity component.

The next section provides background on the method of Lagrangian analysis employed in the study. Following this the computational aspects of the approach, including that of the channel flow simulation and particle data sets, are given. The chief results concerning the physics of Reynolds stress are then presented, including the evaluation of the transport decomposition and descriptions of the typical fluid particle motions in the wall region leading to displacement and acceleration

transport. An overall assessment of the mechanisms leading to momentum transport is then made and some of the implications of this for the modelling of Reynolds stress are described. In the last section conclusions are given together with an outline of future work.

2. Reynolds stress analysis

A Lagrangian decomposition of the Reynolds shear stress, \overline{uv} , at a fixed spatial point, \mathbf{a} , at a given time, t_0 , in a turbulent channel flow may be derived following an approach presented in detail elsewhere (Bernard *et al.* 1989*a, b*). In essence, one substitutes for u an expression deduced from integrating the streamwise component of the Navier–Stokes equation along an arbitrary particle path terminating at \mathbf{a} , at time t_0 . Denoting the initial point of the path at time $t_0 - \tau$, $\tau > 0$, as \mathbf{b} , which will vary randomly from realization to realization of the flow field, the decomposition takes the form

$$\overline{u_a v_a} = \overline{u_b v_a} + \overline{v_a(\overline{U}_b - \overline{U}_a)} - \int_{-\tau}^0 \frac{1}{\rho} \overline{v(0) \frac{\partial p}{\partial x}(s)} ds + \int_{-\tau}^0 \overline{\nu v(0) \nabla^2 U(s)} ds. \quad (1)$$

Here, u is the streamwise and v the wall-normal velocity fluctuation, U is the total streamwise velocity, p the pressure, ρ the density, the subscripts a and b denote quantities evaluated at \mathbf{a} , t_0 and \mathbf{b} , $t_0 - \tau$, respectively, and the overbar indicates ensemble averaging. The notation $U(s)$ is adopted to indicate quantities evaluated along the particle path at time s , and, without loss of generality, t_0 is considered to be 0.

The further step may be taken of substituting for \overline{U}_b in (1) its Taylor series expansion

$$\overline{U}_b = \overline{U}_a - \int_{-\tau}^0 v(s) ds \frac{d\overline{U}}{dy}(a) + \frac{1}{2} \int_{-\tau}^0 \int_{-\tau}^0 v(s)v(r) ds dr \frac{d^2\overline{U}}{dy^2}(\theta), \quad (2)$$

where for each realization of the flow field, θ denotes a different point on the path between \mathbf{b} and \mathbf{a} . This yields

$$\overline{u_a v_a} = \overline{u_b v_a} - \int_{-\tau}^0 \overline{v(0)v(s)} ds \frac{d\overline{U}}{dy} + \Phi_1 + \Phi_2, \quad (3)$$

where

$$\Phi_1 = - \int_{-\tau}^0 \frac{1}{\rho} \overline{v(0) \frac{\partial p}{\partial x}(s)} ds + \int_{-\tau}^0 \overline{\nu v(0) \nabla^2 U(s)} ds \quad (4)$$

and

$$\Phi_2 = \frac{1}{2} \frac{d^2\overline{U}}{dy^2}(\theta) \int_{-\tau}^0 \int_{-\tau}^0 \overline{v(0)v(s)v(r)} ds dr. \quad (5)$$

As τ increases, the magnitude of the first term on the right-hand side of (3) reduces to zero as was demonstrated in earlier work (Bernard *et al.* 1989*a, b*). The second term on the right-hand side accounts for mean gradient diffusion of momentum. It contains an explicit expression for the eddy viscosity in the form

$$\nu_T = \int_{-\tau}^0 \overline{v(0)v(s)} ds, \quad (6)$$

which, in view of the properties of $\overline{v(0)v(s)}$, will be positive. The terms Φ_1 and Φ_2 , defined in (4) and (5), respectively, represent non-gradient transport processes which

are potentially important sources of Reynolds stress. The previous study found both of these to be significant at the point $y^+ = 15.8$. Term Φ_1 represents Reynolds stress arising from a correlation between the fluctuation v_a and changes in the momentum of fluid particles, i.e. accelerations or decelerations, caused by the action of pressure and viscous forces. The remaining term, Φ_2 , reflects a correction to gradient transport caused by the motion of fluid particles over distances greater than that at which a local linear approximation to \bar{U} can be justified.

Implicit in the early analysis of Prandtl is the concept of the mixing time, i.e. the time period over which particles must travel until their momentum is in some sense blended in with the surroundings. The existence of a mixing time is also fundamental to the present approach. It was suggested previously (Bernard *et al.* 1989*a*) that this scale may be naturally associated with the time interval τ until u_b and v_a become uncorrelated, i.e. $\overline{u_b v_a} = 0$ in (3), since it takes this long for the dynamical processes of the flow field to create, in a sense, the Reynolds stress correlation. A closer inspection of (3), however, suggests that a more fundamental definition of mixing time may be discerned. In particular, it may be seen that there must be a threshold in τ beyond which all of the terms in (3) are constants independent of τ . To see this, note that as τ increases, $v(0)$ and $v(\tau)$ becomes less correlated so that eventually ν_T given by (6) becomes constant and so too does the gradient term in (3). Similarly, the correlation of $v(0)$ with $\partial p/\partial x(-\tau)$ and $\nabla^2 U(-\tau)$ will be zero after τ exceeds a certain lower bound. In this case Φ_1 will then be constant. Clearly, the remaining term, Φ_2 , will be constant once τ is large enough to make all the other terms constant. The time, say τ^* , when this is first achieved may be taken as a precise definition of the mixing time. This scale is intrinsic to the turbulent flow field at any point. For $\tau > \tau^*$, (3) produces a fundamental decomposition of the Reynolds stress into its constituent physical processes. By examining these, it is possible to learn a considerable amount about the physics of turbulent momentum transport and the Reynolds stress.

Equation (3) was derived from the point of view of specifically identifying a term responsible for gradient transport. This required applying (2) so as to subdivide the correlation $v_a(\bar{U}_b - \bar{U}_a)$ into gradient and non-gradient components. This step is a mathematical artifice which is not necessarily beneficial either to representing the physics of the Reynolds stress, or as an aid to its modelling. In fact, it will become apparent below that (1), which may be rewritten in the form

$$\overline{u_a v_a} = \overline{u_b v_a} + v_a(\bar{U}_b - \bar{U}_a) + \overline{v_a(U_a - U_b)} \quad (7)$$

since the last term is just Φ_1 , permits a more natural and straightforward analysis of the Reynolds stress than does (3). This equation will be seen to offer some important conceptual advantages in explaining the physics of turbulent momentum transport, and in developing closure relations.

Equation (7) suggests that the Reynolds stress should be looked at as arising from two fundamental processes. The first, which is encompassed by the middle term on the right-hand side, is just the transport mechanism described by Prandtl, wherein v_a is correlated with the change in the mean velocity between a fluid particles' initial and final location. Intrinsic to this term is the idea that the velocity fluctuation u_a arises simply from the fluid particle at point b bringing to point a , on average, the mean momentum of its starting location. For the purpose of the following discussion this transport mode will be referred to as transport by fluid particle displacements. It has been pointed out by Tennekes & Lumley (1972) that this mechanism, as it was envisioned by Prandtl, suffers from the contradiction of requiring both complete

mixing at the end of the mixing time, yet also transfer of momentum unchanged from one position to another. It should be apparent that (7) offers a framework for sorting out this paradox, since, within the context of continuous changes in the momentum of fluid particles, it allows for both the notion of complete mixing as discussed above, as well as diffusion according to Prandtl's conception.

A very different type of transport is represented by the last term in (7). This incorporates the correlation of v_a with the total change in momentum along particle paths, i.e. the acceleration and deceleration of fluid particles. Consequently, it will be convenient to refer to this effect as transport associated with fluid particle accelerations. The suggestion that this type of transport may be significant was put forth by Taylor (1915) as a reason for rejecting a gradient transport model of the kind which was later to be developed by Prandtl. It is evident from (3) that both viscous and pressure forces acting either separately, or in concert, can potentially contribute to acceleration transport.

The two transport mechanisms represented in (7) may, in principle, be of significance at a particular point in the flow independently of one another. Displacement transport should occur generally in the presence of a mean shear, while the circumstances under which acceleration transport should exist is less obvious. An important outcome of the present study will be to reveal some of the occasions when the latter will be of consequence. In general, it will be shown that different types of particle motions are associated with each of the transport mechanisms, though they may have a common origin in the dynamics of vortical structures in the turbulent wall layer.

3. Computational technique

The particle trajectories used in the present study were obtained from a direct numerical simulation of channel flow at Reynolds number $R_\tau = 250$, based on friction velocity and channel width. In terms of the centreline velocity the Reynolds number is 4274. A relatively low value of R_τ was chosen with a view towards obtaining an acceptable simulation on a mesh with fewer points than would be needed at higher values of R_τ . In particular, for the present study a grid with $32 \times 65 \times 64$ mesh points in the streamwise, wall-normal and spanwise directions, respectively, was used. By so reducing the storage requirements necessary to hold each realization of the velocity field in computer memory, the manageability of computing particle paths backward in time was enhanced.

The turbulent field was simulated by solving the Navier–Stokes equations in rotation form subject to the incompressibility condition and no-slip boundary conditions. A forcing term in the momentum equation was chosen in such a manner as to act like a constant pressure gradient driving the flow to a statistically steady state. Numerical solutions to the governing equations were obtained using a pseudospectral method in which Chebyshev polynomials are used in the wall-normal direction, and Fourier series in the streamwise and spanwise directions.

A time-splitting scheme incorporating the Green's-function approach developed by Marcus (1984) was employed to obtain numerical solutions. This technique is a modification of the Orszag–Kells (1980) algorithm in which time-splitting errors inherent in that method are significantly reduced by forcing a divergence-free velocity field at the wall. The code that has been used for the current calculations was originally written by John McLaughlin (Azab & McLaughlin 1987) and has been extensively modified to make it more memory efficient. The present calculations were

initialized from a previous simulation which was known to be nearly statistically steady. Dealiasing of the computed solution was done in the horizontal wavenumber plane using the '3/2' rule so that each of the 64×16 complex modes in the horizontal plane was fully populated. The domain size in wall units was 625 in the streamwise and spanwise directions and 250 in the wall-normal direction. The mean properties of the computed velocity field were comparable in quality to that of other simulations. For example, the constants A and B in the expression for the law of the wall, $\bar{U}^+ = A \ln y^+ + B$, were found to be 2.5 and 5.5, respectively, and the ratio of centreline to bulk mean velocity was 1.17 compared to 1.18 found by Kim, Moin & Moser (1987). Details of the channel flow solution have been reported elsewhere by Handler, Hendricks & Leighton (1989).

The ensembles of paths used in the current study consist of the trajectories of 1000 particles with end points on each of the six planes $y^+ = 3.8, 7.3, 12.0, 17.8, 24.6,$ and 36.6 . In each case, 500 particles were obtained from the flow in the lower half of the channel and 500 in the upper half. The total simulation time of the paths was $\tau^+ = 32$. They were computed by first storing 640 consecutive realizations of the velocity field on magnetic tapes and disk files at intervals $\Delta t^+ \equiv \Delta t U_\tau^2 / \nu = 0.05$. The final positions of the particles were randomly placed in the planes and the particle locations earlier in time were determined by integration through the velocity realizations taken in reverse order. A second-order Runge-Kutta scheme was used to perform the time integration.

The accuracy of the paths was assessed by computing the motion of all the particles from their positions at time $t^+ = -\tau^+$ forward in time over the identical 640 flow records until $t^+ = 0$. Denoting the backward and forward paths by $X_b(\mathbf{a}, t)$ and $X_f(\mathbf{a}, t)$, respectively, then by definition, $X_b(\mathbf{a}, 0) = \mathbf{a}$ and $X_f(\mathbf{a}, -\tau^+) = X_b(\mathbf{a}, -\tau^+)$. The root-mean-square difference

$$\epsilon(t^+) \equiv \left\{ \frac{1}{N} \sum_{i=1}^N |X_f^i(\mathbf{a}, t^+ - \tau^+) - X_b^i(\mathbf{a}, t^+ - \tau^+)|^2 \right\}^{\frac{1}{2}},$$

where $N = 1000$, between the backward and forward positions of the particles was calculated. Figure 1 contains a plot of $\epsilon(t^+)$ for each y^+ level as a function of time. It is seen that on average the particles return to within a very small distance of their starting points. For example, in the worst case, which is for the paths which end at $y^+ = 36.6$, the root-mean-square error is $< 10^{-4}$ as measured in viscous units. It is also evident that these errors are rapidly increasing with time so that for longer time intervals they may become significant.

An additional source of error in the particle paths arises from the use of three-dimensional linear interpolation to find the velocities of particles at off-nodal points (Yeung & Pope 1988). An extensive study of how such errors affect the accuracy of the current paths was carried out by comparing paths computed using linear interpolation with those computed using exact spectral interpolation. For the near-wall region considered in the present study it was found that the mesh cell size was sufficiently small that particle paths generated by the linear scheme were essentially indistinguishable from those derived from the exact formula.

Ensemble averages are estimated in the present work by taking averages over the sets of paths. Clearly, this introduces a statistical error depending on both the sample size, i.e. the number of paths in the ensemble, as well as the degree of independence of the paths in the data set. The large number of particles, 1000, used at each y -level, is enough to ensure a relatively low variance in the average properties computed from the ensembles. The final points of the paths are distributed on each y -plane at

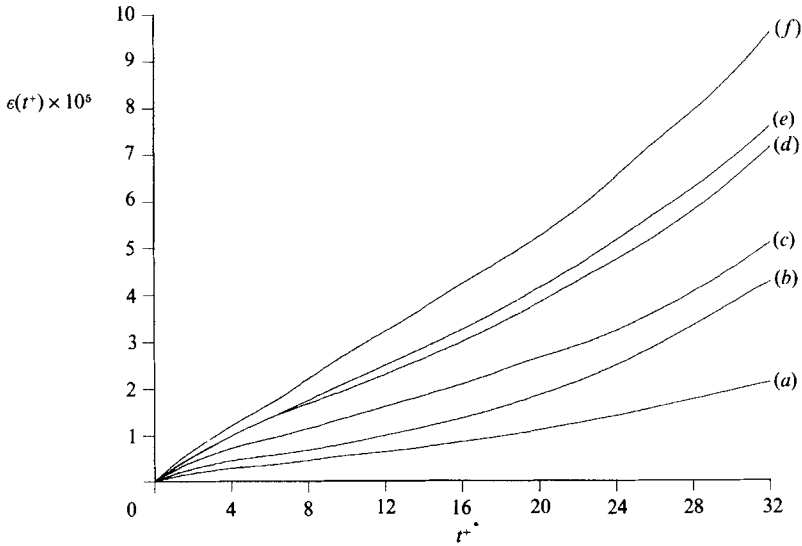


FIGURE 1. Root-mean-square positional errors for computed particle paths: (a-f) correspond to $y^+ = 3.8, 7.3, 12.0, 17.8, 24.6$ and 36.6 , respectively.

the density of approximately one for every fourth cell in the planar mesh. Including more paths computed over the same time interval of the simulation was found to have only a minor quantitative affect on the statistics. This indicates that such paths do not offer much in the way of additional statistically independent information.

To obtain an ideal set of paths for the current analysis, i.e. one whose averages would be equal to the theoretically exact averages, requires having paths separated in time as well as in space. In this way statistical information from the complete simulated velocity field could be brought into the ensemble of paths. Unfortunately, practical considerations preclude obtaining this kind of data. In particular, this would considerably magnify the already formidable task of storing and retrieving the data contained in just one contiguous set of 640 velocity records. However, by incorporating data sets from both walls of the channel, as was done here, it was possible to augment the statistical independence of the paths without great additional cost. The statistics for the combined set of data including both the top and bottom of the channel are given here. These are not substantially different from those taken from the separate data sets. Consequently, it is unlikely that the results of the present study would be much different if a larger, more statistically independent ensemble of paths were used.

4. Overview of Reynolds stress decomposition

According to the discussion in §2, the decomposition of \overline{wv} given in (3) will be useful only if τ exceeds the mixing time. Consequently, it is necessary to check that this condition is satisfied before considering the predicted values of the terms in (3). A plot of the time history of the $\overline{u_b v_a}$ correlation normalized by \overline{uv} , at the different y^+ locations, is shown in figure 2. It is seen that of the six positions treated in the current study, $\overline{u_b v_a}$ essentially reached zero at the four points for which $y^+ \geq 12$, while for $y^+ = 7.3$, it was reduced to less than 20% of its initial value. At the point closest to

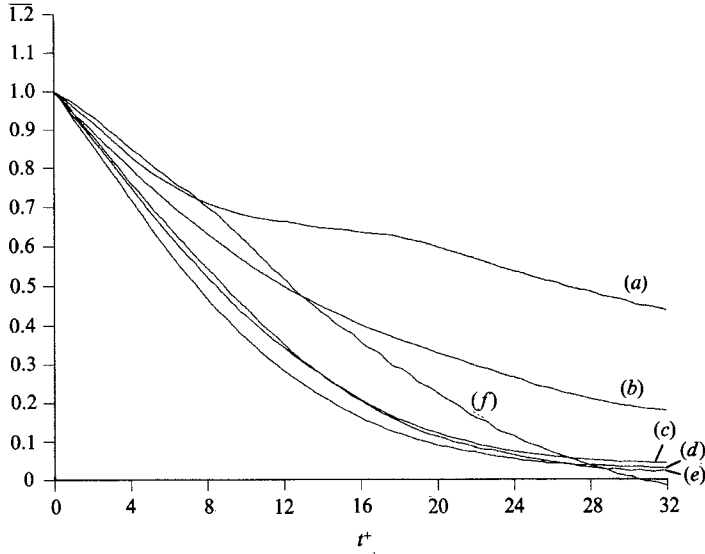


FIGURE 2. Time development of $\overline{u_b v_a}$ correlation for each ensemble of paths: (a-f) correspond to $y^+ = 3.8, 7.3, 12.0, 17.8, 24.6$ and 36.6 , respectively.

the wall, $y^+ = 3.8$, $\overline{u_b v_a}$ was only approximately halfway to zero. Similar behaviour was found regarding the constancy of the remaining terms in (3). Away from the wall they were either constant or nearly so, while near the boundary they were still evolving at $\tau^+ = 32$. This suggests that the total simulation time of $\tau^+ = 32$ is sufficient for complete mixing everywhere except very close to the wall.

The subsequent results will make it clear that the fluid particle motions associated with sweep events, i.e. $u_a > 0, v_a < 0$, commonly experience substantial decelerations as they enter the near-wall region. For such paths it is expected that u remains positive over a significant time interval prior to t_0 . In this case, a large contribution to the product $u_b v_a$ is likely which can explain the persistence of the $\overline{u_b v_a}$ correlation adjacent to the boundary. Fortunately, because of the very small magnitude of the Reynolds stress at $y^+ = 3.8$, the failure of $\overline{u_b v_a}$ to be close to zero at this point will turn out to be of only minor consequence for the following discussion.

A numerical evaluation of the Reynolds stress decomposition given in (3) obtained from the particle paths at all six locations is summarized in figure 3. The magnitude of $\overline{u_b v_a}$ is seen to be uniformly small across the region so that the decomposition of \overline{uv} into the remaining terms in (3) is meaningful. Note that at $y^+ = 3.8$, even though $\overline{u_b v_a}$ still accounts for a large fraction of \overline{uv} , it is very small relative to the peak magnitude of the Reynolds stress distribution. This suggests that any conclusions about the physics of the Reynolds stress which may be deduced from the figure will not be significantly affected if a larger value of τ^+ were used near the boundary.

A striking feature of figure 3 is the behaviour of the gradient transport term with respect to the Reynolds stress itself. The former exceeds the latter in magnitude for $y^+ \leq 20$, and is less than it for the region $y^+ > 20$. This result is consistent with the earlier study (Bernard *et al.* 1989*a*). Extrapolation of the curves in figure 3 towards the centreline suggests that gradient transport will continue to diminish in importance with respect to the total Reynolds stress as the central region of the channel is approached. Figure 3 shows that Φ_2 in (3) is positive near the wall so that it counterbalances the tendency of the gradient term to overestimate the Reynolds

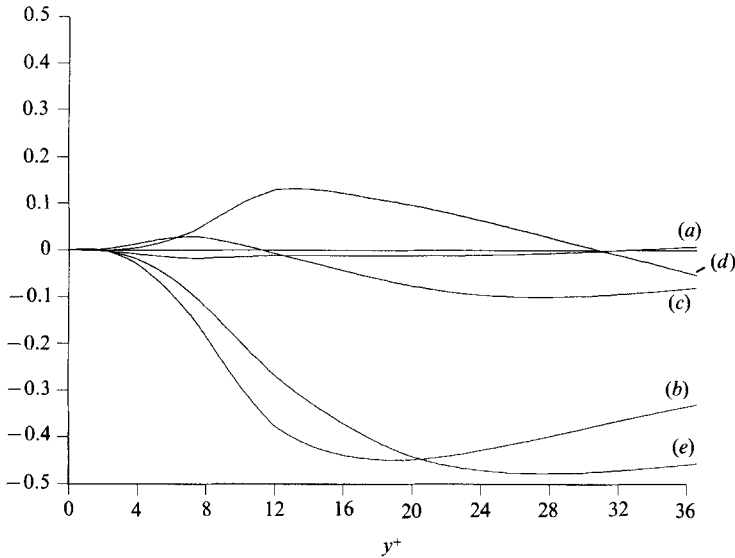


FIGURE 3. Spatial dependence of terms in Reynolds stress decomposition (3): (a) $\overline{u_b v_a}$; (b) gradient term; (c) Φ_1 ; (d) Φ_2 ; (e) \overline{wv} .

stress. Near $y^+ = 30$, Φ_2 changes sign so that beyond this point it acts in the manner of an additional source of Reynolds stress. Term Φ_1 is observed to contribute positively to \overline{wv} for $y^+ \leq 12$ while it makes a somewhat constant negative contribution to Reynolds stress further from the wall.

It may be concluded from figure 3, in agreement with earlier work, that the physical effects accounted for by the terms Φ_1 and Φ_2 constitute a significant aspect of the physics of the Reynolds stress, and therefore cannot be neglected in favour of a simple gradient transport model. To further the specific aims of the present study it is thus necessary to delve more deeply into the physical processes represented by these terms. A step in this direction was taken previously (Bernard *et al.* 1989*a, b*) when it was established that non-gradient transport effects are largely attributable to the motion of a small number of exceptional particles travelling long distances during the mixing time. Here, many refinements to this observation will be made as the connection between particle motions and Reynolds stress is further mapped out.

5. Analysis of particle paths

For the purpose of developing a physical picture of the Reynolds stress it is helpful to study the contributions which particular subgroups of paths make to the terms in (3). It turns out to be especially useful to subdivide the paths according to both their initial positions in the y -direction and the quadrant in the (u, v) -hodograph plane they are in at their termination point. In the following, the paths will be considered according to these two criteria applied either separately or together as the situation warrants.

Before considering the relationship between specific attributes of trajectories and the results contained in figure 3, it is advantageous to examine some of the basic statistics of the computed particle paths. In particular, the probability density function (p.d.f.), $p(y)$, corresponding to the initial positions of the particles as

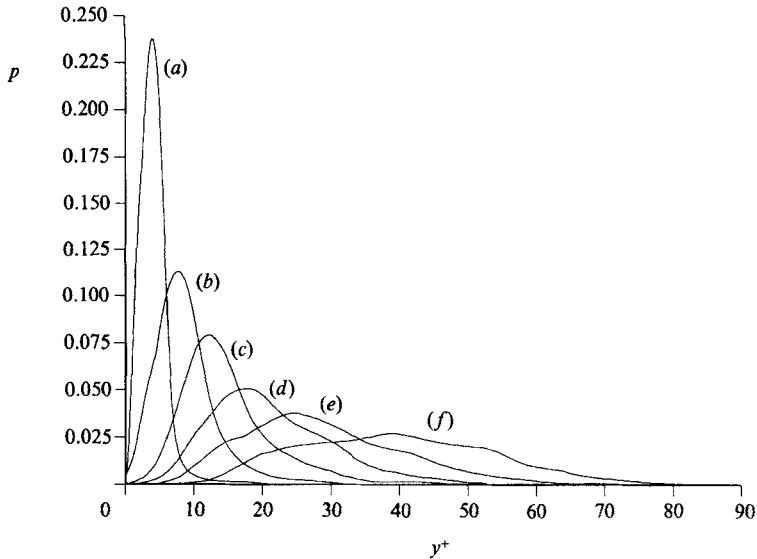


FIGURE 4. Probability density functions of initial particle positions: (a-f) correspond to $y^+ = 3.8, 7.3, 12.0, 17.8, 24.6$ and 36.6 , respectively.

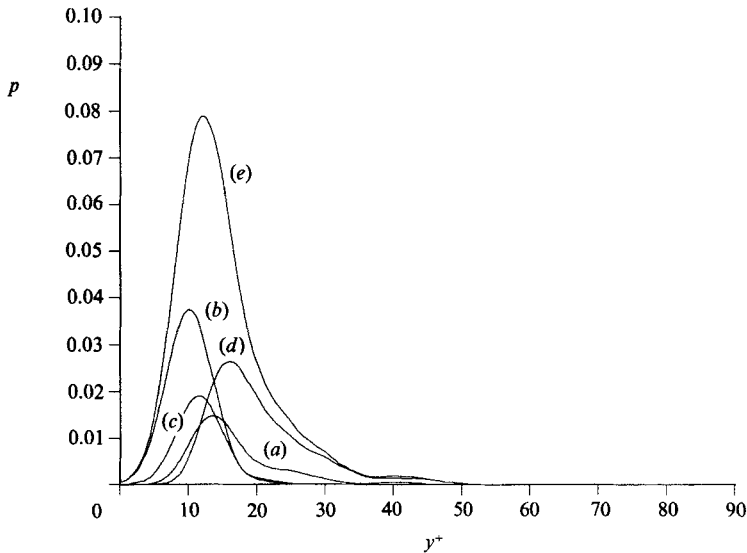


FIGURE 5. Quadrant breakdown of the p.d.f. of particle displacement at $y^+ = 12.0$: (a) Q1; (b) Q2; (c) Q3; (d) Q4; (e) total.

measured from the wall, for each of the six y -locations, is shown in figure 4. These were computed by first evaluating the cumulative probability distribution function $P(y) \equiv \int_{-\infty}^y p(z) dz$, at a set of discrete points, and then setting $p(y)$ equal to the slope of a straight line fitted to P in the vicinity of y . As expected, the least spread of initial states is for the paths that end at $y^+ = 3.8$, while the greatest is for those arriving at $y^+ = 36.6$. At each y^+ location the most probable initial state is approximately

coincident with the final state. However, the $p(y)$ curves are asymmetric about the most probable location with the longer tail extending in the direction away from the channel wall. This suggests that the mean y -location for each ensemble of paths should be drifting towards the wall. Direct calculation reveals that this is indeed the case.

Considerable insight into the dynamics of the wall region can be had by performing a quadrant analysis of the curves in figure 4 along the lines discussed previously. Such a breakdown of the particular curve in figure 4 at $y^+ = 12$ is shown in figure 5. It is seen that, as expected, Q2 events, i.e. particles for which u_a, v_a are in quadrant 2 ($u_a < 0, v_a > 0$) of the hodograph plane, are most likely to have originated closer to the wall than $y^+ = 12$, while Q4 events are most likely to have approached the wall from further away. Q2 and Q4 events are also seen to be much more numerous than Q1 or Q3 events. It may be observed that for all of the four groups of paths, there are many which begin their travel from locations opposite to ones' expectation of where they should start judging solely by the sign of v_a . In other words, a significant fraction of the particle paths change their direction over the mixing time.

An especially interesting feature of figure 5 is that a very high percentage, in fact, 76% of the Q1 events undergo a change in direction. Visualizations of these paths along the lines done in the earlier study (Bernard *et al.* 1989*b*) show that many of them follow arcing trajectories in which they descend towards the wall very much like sweep motions, but become reoriented upwards prior to time t_0 . In general, these particles travel faster than the local mean at $y^+ = 12$ so that the source of a positive fluctuation, u_a , lies in their origin in the high-speed region further from the wall.

As in the case of Q1 events, figure 5 shows that slightly more than half, namely 53%, of all Q3 events begin travelling outward from close to the wall and then change direction back towards the wall. These also may be seen to be largely spiral motions in which u_a is negative owing to the fluid particle's previous passage close to the wall. Taken as a whole, it is seen that Q1 and Q3 particle trajectories give the appearance of being the culminating behaviour of sweep and ejection events, respectively, in which particles change direction because of their association with the motion of vortical structures in the wall region. It should be noted that a similar scenario was proposed by Brodkey, Wallace & Eckelmann (1974) in their interpretation of experimentally observed particle paths.

It may be concluded that the positive fluctuation u_a associated with Q1 and Q4 events signifies that the fluid particle is highly likely to have originated farther from the wall than its final position. Similarly, $u_a < 0$, occurring in Q2 and Q3 events, most often means that the particle path started in the slow-moving region close to the wall. These general conclusions also apply to the paths at locations other than $y^+ = 12$, since the remaining curves in figure 4 have quadrant breakdowns similar to that shown in figure 5.

6. Transport by fluid particle displacements

The computed trends in the gradient and Φ_2 terms in figure 3 are a natural consequence of the relationship between the particle motions occurring during the mixing time and the properties of the mean velocity field. By exploring this connection, a considerable amount can be revealed about the physics of momentum transport. The present discussion considers the gradient term together with the non-gradient process represented by Φ_2 , since together they form the correlation $v_a(\bar{U}_b - \bar{U}_a)$. This term, as suggested previously, corresponds mathematically to the

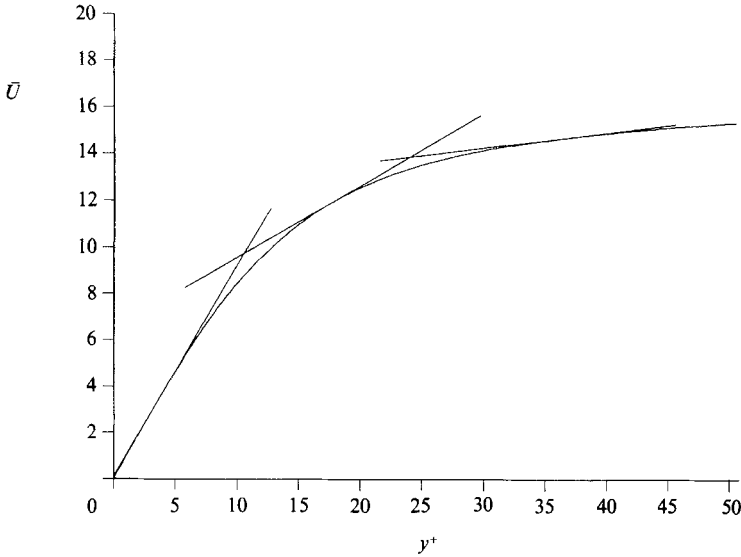


FIGURE 6. Mean velocity profile in channel flow showing the suitability of linear approximations.

physical process described by Prandtl in which u_a is treated as if it were created entirely by the mean velocity at point b being brought to point a by the displacement of fluid particles.

The association between the mean velocity field and the gradient and Φ_2 terms can be understood with the help of figure 6, containing a plot of \bar{U} upon which is superimposed tangent lines at the three points $y^+ = 3.8, 17.8$ and 36.6 . Consider the dynamics of typical fluid particles causing momentum transport across the plane at $y^+ = 17.8$. For a particle having $v_a > 0$, and $y_b^+ < y_a^+ = 17.8$, i.e. that originated at a position b closer to the wall, $\bar{U}_b - \bar{U}_a$ will be negative. According to (2), $\bar{U}_b - \bar{U}_a$ can be decomposed into a sum of contributions from the linear approximation to \bar{U} through a , plus a higher-order correction. The relative positions of the curves in figure 6 at a hypothetical point y_b^+ , situated somewhat to the left of y_a^+ , make it evident that the part of $\bar{U}_b - \bar{U}_a$ deriving from the linear approximation to \bar{U} will be negative, and will account for only a part of the total difference, $\bar{U}_b - \bar{U}_a$. The remaining contribution to $\bar{U}_b - \bar{U}_a$ comes from the higher-order term in (2) which may be seen to also be negative. Since the gradient term in (2) is composed of the correlation of v_a with the gradient part of $\bar{U}_b - \bar{U}_a$, it follows that particles with $v_a > 0, y_b^+ < y_a^+$, tend to contribute less in magnitude to gradient transport than they do to the overall local Reynolds stress. In addition, since Φ_2 is formed as the product of v_a with the higher-order term in (2), it will receive a negative contribution from this kind of particle motion.

Now consider the equivalent situation, but for a particle for which $v_a < 0$ and $y_b^+ > y_a^+$. In this case $\bar{U}_b - \bar{U}_a$ will be positive. Examination of the curves in figure 6 just to the right of $y^+ = 17.8$ reveals that, unlike the previous instance, the linear term in (2) will now tend to be larger in magnitude than $\bar{U}_b - \bar{U}_a$, while the part of $\bar{U}_b - \bar{U}_a$ coming from the higher-order correction in (2) will counterbalance this by being negative. It thus happens that for particles approaching the wall, it is expected that their contribution to the gradient term in (3) will exceed in magnitude that of their

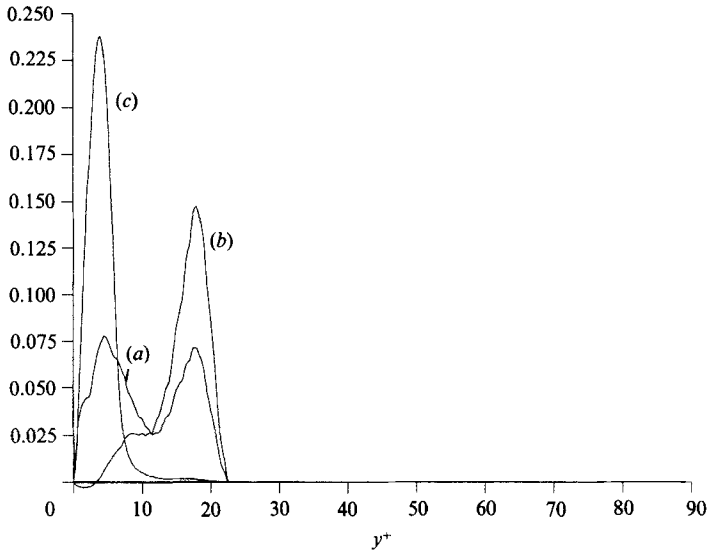


FIGURE 7. Computed probability density functions at $y^+ = 3.8$: (a) gradient term; (b) Φ_2 ; (c) initial positions of particles.

contribution to the Reynolds stress, while at the same time they contribute positively to Φ_2 .

In summary, in so far as the gradient term in (3) is concerned, particles moving away from the wall tend to contribute less to it in magnitude than they do to the local Reynolds stress, while particles moving towards the wall tend to contribute more in magnitude to it than they do to the Reynolds stress. For the term Φ_2 , outward-moving particles contribute negatively, i.e. so as to enhance the local Reynolds stress, while those moving inward contribute positively, i.e. so as to reduce the total Reynolds stress. In the event that a linear approximation to \bar{U} is acceptable over the distance at which fluid particles move over the mixing time, then the higher-order term in (2) will be negligible and Φ_2 can be expected to be zero. In contrast, the gradient term will contribute to Reynolds stress in all circumstances, so long as $d\bar{U}/dy \neq 0$.

At this point it is possible to readily explain the behaviour of the gradient and Φ_2 terms shown in figure 3. First consider the region near the wall. It may be seen in figure 6 that a linear approximation to \bar{U} at $y^+ = 3.8$ is excellent for particles travelling outward towards $y^+ = 3.8$, while it is not particularly good for particles heading inward to $y^+ = 3.8$. In view of the previous discussion, it may be expected that the gradient term will overpredict the Reynolds stress at this point since the Q4 particles travelling to $y^+ = 3.8$ from above make excessive contributions to gradient transport without a compensating underprediction from outward-moving particles. Similarly, the curves in figure 6 at $y^+ = 3.8$ suggest that the main contribution to Φ_2 is from particles moving to the wall, since the correction to the gradient approximation to \bar{U} for outward-moving particles will be negligible. The net result is that Φ_2 should be positive, as is shown to be the case in figure 3.

An instructive view of the conclusions just reached is given in figure 7, containing a plot of the p.d.f.'s associated with the gradient and Φ_2 terms in (3) at the point $y^+ = 3.8$, as well as the p.d.f. of particle displacement. The former curves, at a fixed y ,

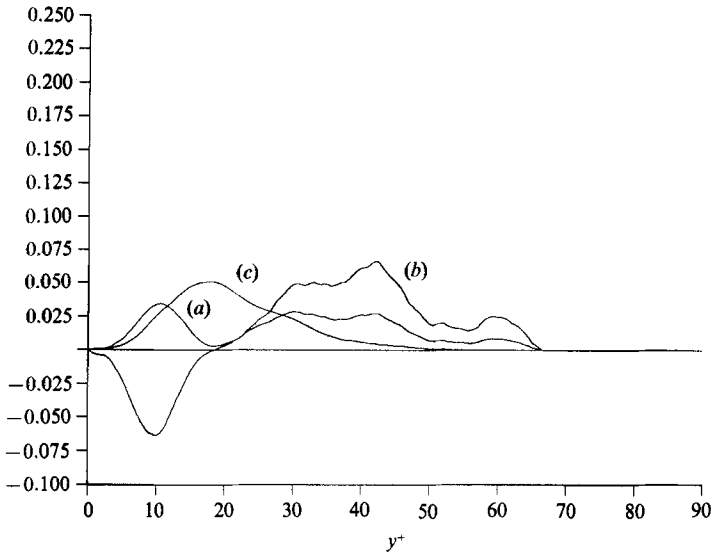


FIGURE 8. Computed probability density functions at $y^+ = 17.8$: (a) gradient term; (b) Φ_2 ; (c) initial positions of particles.

give the fraction of the total gradient and Φ_2 terms, respectively, stemming from particles originating near y and travelling to $y^+ = 3.8$. It is evaluated in the same manner by which the p.d.f. of particle displacement was computed, namely by differentiation of the associated cumulative probability function, $P(y)$. Since it is possible that particles originating from a particular location may tend to contribute opposite in sign to that of the net value of the term, it cannot be ruled out that there are regions where $p(y)$ is negative. In all cases, however, the integral of $p(y)$ over all y is unity.

Figure 7 reveals the remarkable extent to which a very large portion of the gradient contribution to Reynolds stress, and almost the entire contribution to Φ_2 , come from the small number of particles travelling to $y^+ = 3.8$ from positions beyond $y^+ = 10$ from the wall. The most probable contribution to gradient transport is from particles originating near $y^+ \approx 17$, yet, as shown in figure 6, the tangent line to \bar{U} at $y^+ = 3.8$ very poorly approximates \bar{U} in this vicinity. The result, as was made clear in the previous discussion, is that the gradient term will be too large in magnitude, and Φ_2 will be positive.

At points further from the wall, such as $y^+ = 17.8$, the local linear approximation to \bar{U} is a poor representation of \bar{U}_b for both outbound and inbound particles travelling significant distances. Figure 8 shows the p.d.f.'s for the gradient and Φ_2 terms in (3) for particles arriving at $y^+ = 17.8$. As before, the dominant contribution to displacement transport is from a small number of particles travelling relatively long distances during the mixing time. The p.d.f. for the gradient term displays a characteristic profile in which a local maximum occurs on either side of the terminal point. The greatest contributions to gradient transport arise from particles travelling outward from $y^+ \approx 10$ and inward from $y^+ \approx 30-45$. The inadequacy of a linear approximation to \bar{U} at $y^+ = 17.8$ in accounting for these contributions is evident in figure 6. However, it may be expected that the tendency towards overprediction of gradient transport by the inward-moving particles will be counteracted by an opposite effect due to the outward-moving particles. Thus a lessening of the

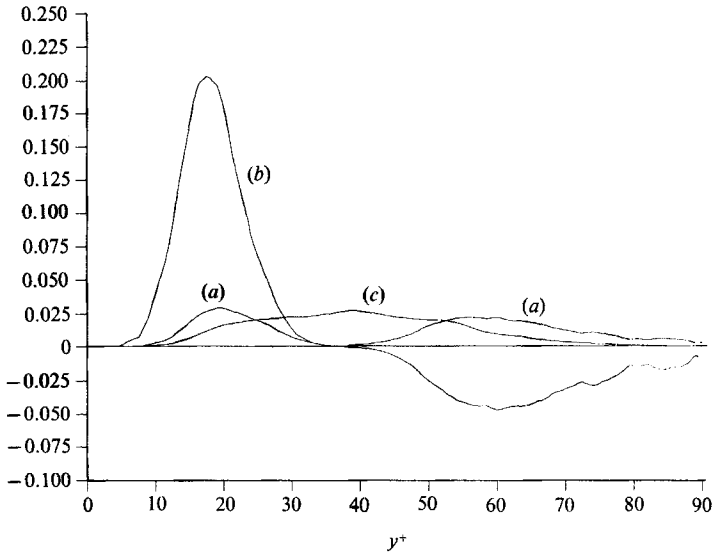


FIGURE 9. Computed probability density functions at $y^+ = 36.6$: (a) gradient term; (b) Φ_2 ; (c) initial positions of particles.

magnitude of the gradient term with respect to the Reynolds stress should occur. Figure 3 shows that, in fact, at $y^+ \approx 20$ the gradient term begins to underpredict the Reynolds stress.

The increasing importance of outward-moving particles at $y^+ = 17.8$ is made evident by the p.d.f. for Φ_2 . Here it is seen that these particles make a sizeable negative contribution to Φ_2 , cancelling some of the positive contribution from inward-travelling particles. This explains the decrease in Φ_2 for $y^+ > 12$ evident in figure 3. At $y^+ \approx 30$ the positive and negative contributions to Φ_2 fully balance so that it is zero. Beyond this point the negative contributions from outward-moving particles dominate and Φ_2 becomes negative.

At $y^+ = 36.6$, figure 6 shows that a situation somewhat opposite to that at $y^+ = 3.8$ occurs. The p.d.f. of the gradient term at $y^+ = 36.6$ shown in figure 9 indicates that the most probable contributions to gradient transport come from particles moving outward from $y^+ \approx 18$ and inward from $y^+ \approx 60$. For the latter particles the linear representation of \bar{U} at $y^+ = 36.6$ is considerably better than for the former, so the gradient term can be expected to fall short of the total Reynolds stress in magnitude. The negative value of Φ_2 at $y^+ = 36.6$ is reflected in the fact that its p.d.f. curve, which is shown in figure 9, is now positive for particles heading outward, and negative for ones moving inward, in contrast to the situation at $y^+ = 17.8$. It also may be concluded from figure 9 that the Reynolds stress, away from the vicinity of the wall, depends on physical processes covering a very substantial part of the channel.

Quadrant analyses of the gradient and Φ_2 transport terms are presented in figures 10 and 11, respectively. Next to the boundary almost the entire contribution to these processes is due to fluid particle motions terminating in Q4. Outside the immediate wall region Q4 events continue to exert a major influence on both facets of displacement transport, though this is mollified somewhat in that they contribute negatively to the gradient and positively to the Φ_2 terms. In contrast, the figures show that Q2 events contribute negatively to both processes and, as will be shown

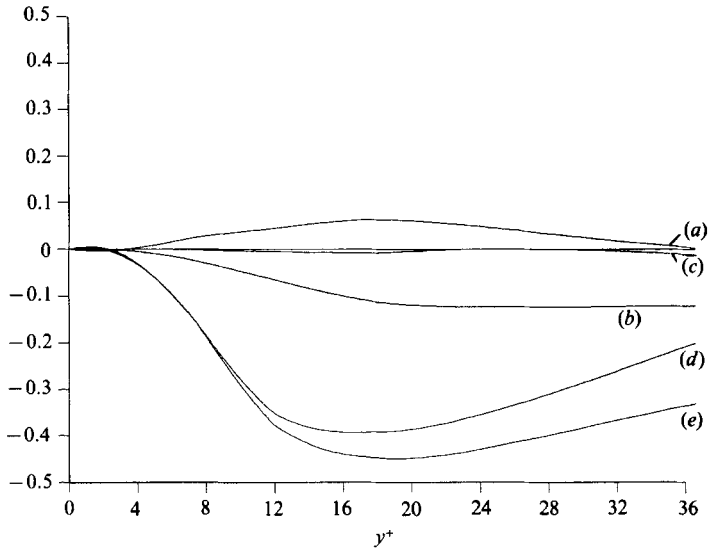


FIGURE 10. Quadrant decomposition of the gradient term in (3): (a) Q1; (b) Q2; (c) Q3; (d) Q4; (e) total.

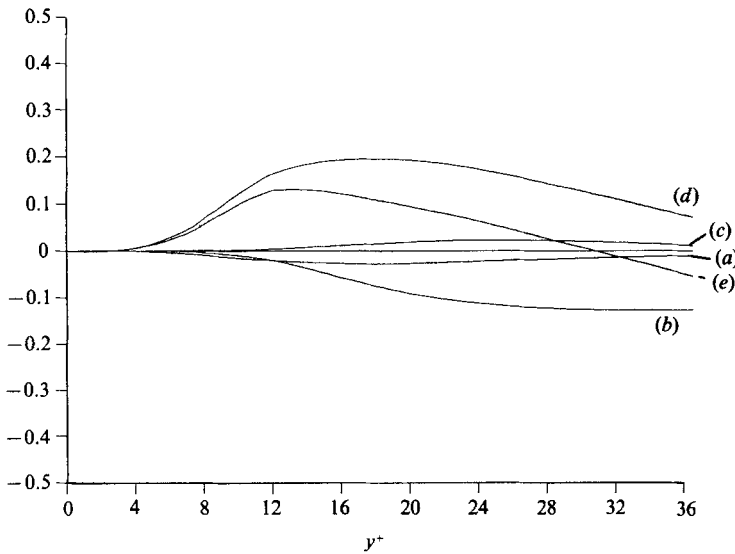


FIGURE 11. Quadrant decomposition of term Φ_2 in (3): (a) Q1; (b) Q2; (c) Q3; (d) Q4; (e) total.

below, come to dominate displacement transport away from the wall. An interesting aspect of figure 10 is that Q1 events appear to be responsible for a sizeable positive contribution to gradient transport. For this to happen, since $v_a > 0$ for such particles, it must generally be the case that $\bar{U}_b > \bar{U}_a$, so that $y_b^+ > y_a^+$. In other words, a change in direction is implied in these motions. The presence of many Q1 paths with this property was established previously.

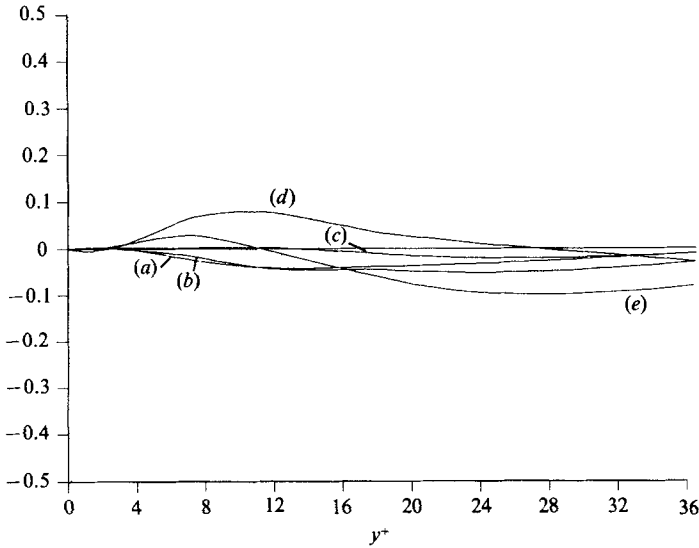


FIGURE 12. Quadrant decomposition of term Φ_1 in (3): (a) Q1; (b) Q2; (c) Q3; (d) Q4; (e) total.

7. Transport by fluid particle accelerations

The behaviour of $\Phi_1 \equiv \overline{v_a(U_a - U_b)}$ shown in figure 3 can also be interpreted in terms of the basic properties of the fluid particle motions. Near the wall where it is positive, a correlation is implied between events in which v_a and $U_a - U_b$ have the same sign. A quadrant breakdown of the acceleration transport term shown in figure 12 reveals that the positivity of Φ_1 near the wall is entirely due to Q4 events. For these paths $v_a < 0$ so it must often be the case that $U_a - U_b < 0$ as well. In other words, the positivity of Φ_1 near the boundary is explained by the deceleration of many sweep motions heading into the near-wall region. The opposite situation, in which ejection motions accelerate, also occurs as will be seen below, though this is of less significance.

Since, according to figure 3, Φ_1 changes sign at $y^+ \approx 12$, the complete set of physical processes underlying this term must be more complex than the simple scheme just proposed. For example, the mechanisms cited to account for positive Φ_1 cannot explain why it is negative, since it is implausible to expect either that many particles leaving from near the wall decelerate or that many particles approaching the wall accelerate. Figure 12 makes clear that the source of negative Φ_1 , near $y^+ = 15$, lies in the motion of paths terminating in Q1 and Q2. Since these events have $v_a > 0$, to contribute negatively to Q1 they must be decelerating. In view of the previous remarks, it appears to be highly likely that a change in direction is involved in these paths. Figure 12 also shows that by $y^+ = 36$, Q3 and Q4 motions contribute negatively to Φ_1 . In this case, there must exist a number of particles which accelerate as they leave from near the wall, and then turn back towards it so that they terminate with $v_a < 0$.

Visualizations of the ten paths, out of the complete set of 1000 paths, contributing most negatively to acceleration transport at $y^+ = 24.6$ are contained in figure 13. The trajectories are displayed in orthogonal projections from the side, top and end-on, as seen by an observer moving at the mean speed at $y^+ = 24.6$. The paths are plotted from a common origin and an equal spatial scaling is used in all coordinate directions.

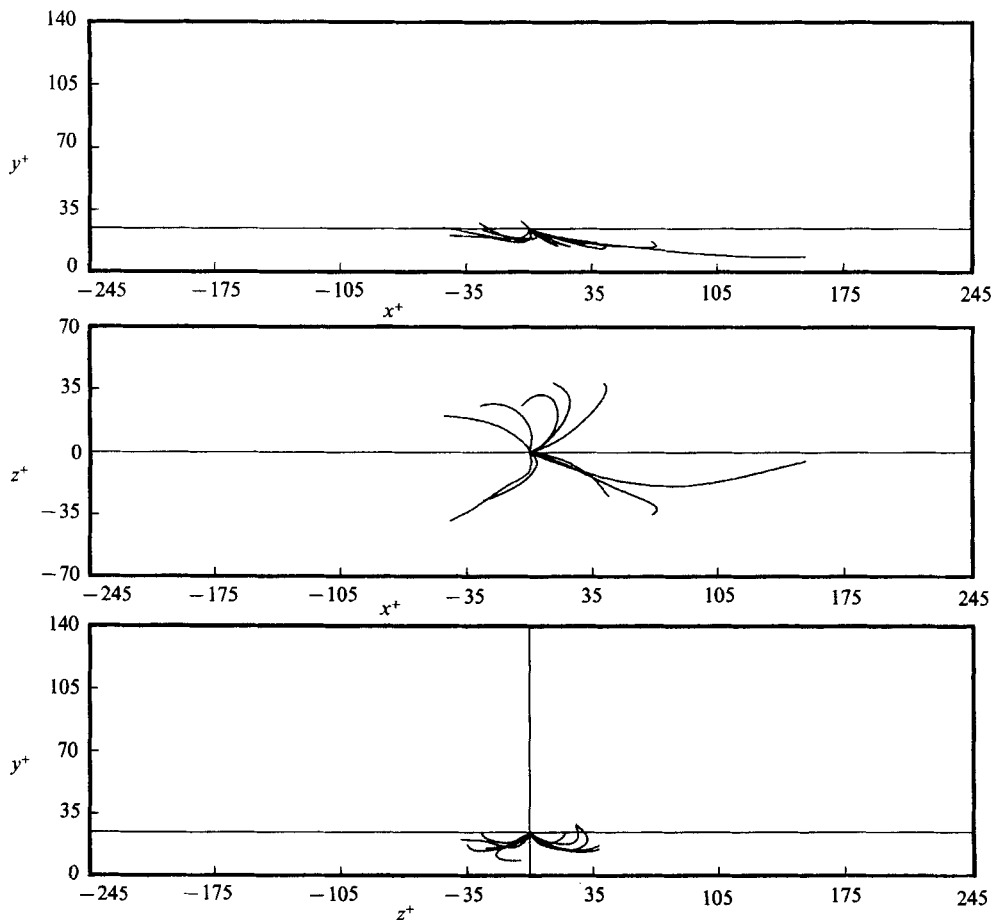


FIGURE 13. Visualizations of particle trajectories. Ten paths contributing most negatively to $\overline{v_a(U_a - U_b)}$ at $y^+ = 24.6$.

Paths to the right of the x^+ origin in the top two figures are travelling slower than the mean, and paths to the left faster. Viewed end-on it is apparent that the particles terminate in Q1 or Q2 so that they are all decelerating. It is also evident that they have undergone a change in direction consistent with the previous discussion.

The paths in figure 13 tend to displace only a small distance in the wall-normal direction over the mixing time. This is consistent with a plot of the p.d.f. of Φ_1 at $y^+ = 24.6$ in figure 14 which shows that $p(y)$ is at a peak at $y^+ = 24.6$. This implies that the most significant source of negative contributions to Φ_1 is from paths which do not travel a large distance normal to the wall. The regions in figure 14 where $p(y)$ is negative are locations where the instantaneous product $v_a(U_a - U_b)$ tends to be positive. Clearly, these paths contribute to Φ_1 by either slowing as they approach the wall ($y^+ > 40$), or accelerating as they leave the wall ($y^+ < 15$), without an implied change in direction.

It is natural to wonder how the particles depicted in figure 13 are able to decelerate to any great extent without having travelled a significant distance towards the fixed boundary. A possible explanation is suggested by the fact that the paths display a clear spiral pattern, as if they are convecting around the cores of vortex tubes tilted

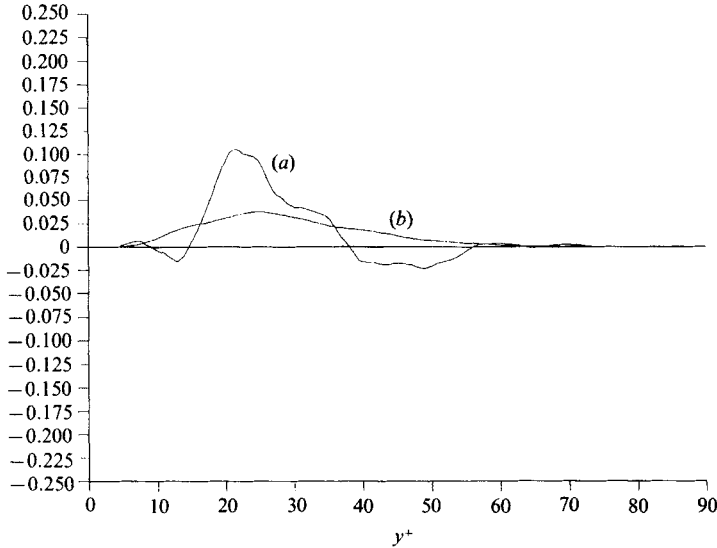


FIGURE 14. Computed probability density functions at $y^+ = 24.6$: (a) Φ_1 ; (b) initial positions of particles.

downstream at an angle to the wall. In particular, the velocity field generated by such structures can be expected to enhance the streamwise velocity on one side and diminish it on the other, so that fluid travelling into such vortices from underneath would tend to decelerate. If these structures form the legs of lifted-up horseshoe or hairpin vortices, then the events being considered represent fluid being drawn into their centres from outside. A similar argument can be provided to explain the acceleration transport generated by Q3 and Q4 events further from the wall. In this case the fluid particles may be heading in an arc around the upper part of the vortex cores.

8. Summary of Reynolds stress physics

At this point a number of conclusions may be drawn about the kinds of physical processes in turbulent flow which lead to the Reynolds stress. First, it is clear from figure 3 that the gradient transport mechanism is a poor estimate of the total Reynolds stress throughout the wall region. By all indications it will be even worse at points further from the wall. Besides its inability to account for the Reynolds stress, it is also inadequate for approximating the total displacement transport term, $v_a(\bar{U}_b - \bar{U}_a)$, of which it is one part. In particular, the inappropriateness of a local linear approximation to \bar{U} in representing \bar{U}_b ensures at the outset that Φ_2 cannot act as merely a small correction to the gradient approximation to $v_a(\bar{U}_b - \bar{U}_a)$. It may be concluded that gradient transport has no intrinsic meaning to turbulent diffusion, so that the subdivision of $v_a(\bar{U}_b - \bar{U}_a)$ into gradient and non-gradient parts serves only to obscure the physics of the Reynolds stress.

The present study thus leads to the notion that it is advantageous to consider the displacement transport process taken as a whole instead of divided into gradient and non-gradient parts. Thus the decomposition of the Reynolds stress given in (7) is preferable to that given in (3). This point of view is supported by figure 15 showing

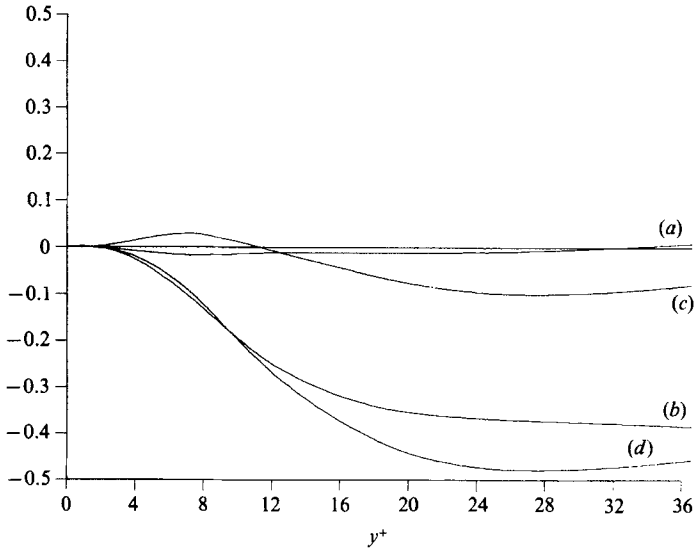


FIGURE 15. Spatial dependence of terms in Reynolds stress decomposition (7): (a) $\overline{u_b v_a}$; (b) $v_a(\overline{U_b} - \overline{U_a})$; (c) $v_a(\overline{U_a} - \overline{U_b})$; (d) \overline{uv} .

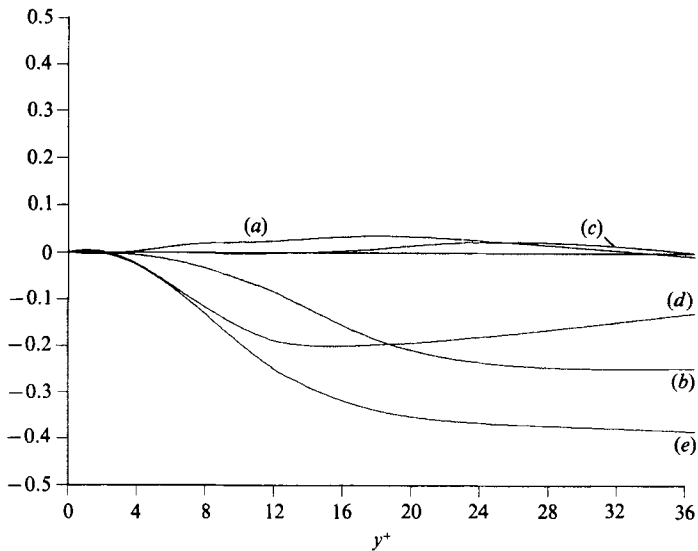


FIGURE 16. Quadrant decomposition of $\overline{v_a(\overline{U_b} - \overline{U_a})}$ in (7): (a) Q1; (b) Q2; (c) Q3; (d) Q4; (e) total.

the distribution of the separate terms in (7) across the channel together with the Reynolds stress. It is evident that $\overline{v_a(\overline{U_b} - \overline{U_a})}$ provides a much more credible approximation to the total Reynolds stress than does the gradient term taken by itself.

A quadrant breakdown of the displacement transport term is shown in figure 16. The dominant role of sweep, i.e. Q4 motions, is evident near the wall. Beyond approximately $y^+ = 18$, as suggested previously, Q2 events involving the ejection of

low-speed fluid away from the wall constitute the major source of displacement transport. According to the figure the net effect of displacement transport is reduced somewhat by the action of Q1 and Q3 paths which have experienced a change in direction over the mixing time.

Acceleration transport has been seen to be the result of two dissimilar mechanisms with different consequences for the overall Reynolds stress distribution. Near the wall it is manifested in the guise of slowing sweep motions and thus leads to a reduction of the Reynolds stress. Further from the wall it acts as an additional source of Reynolds stress by a mechanism consisting of the deceleration of particles travelling in spiral paths first towards and then away from the wall. At more distant points the opposite case occurs in which accelerating particles travel away from and then back towards the boundary. Figures 8, 9 and 14 make the important point that the paths most responsible for displacement and acceleration transport are largely disjoint from each other. The former tend to originate at locations considerably above or below the termination point while the latter begin and end near the same y -level. However, visualizations of the paths most responsible for displacement transport, in agreement with the previous study (Bernard *et al.* 1989*b*), generally show spiral motions covering significant vertical motion, as would be associated with vortical structures more or less aligned with the flow. This together with the previous assessment of the causes of acceleration transport suggests that the two differing sources of turbulent momentum transport have a common origin in the dynamics of largely streamwise vortices in the turbulent boundary layer.

9. Implications for Reynolds stress modelling

Having established in the previous section a comprehensive picture of the sources of momentum transport, it is of interest to now consider some of the implications that this may have on schemes for predicting the Reynolds stress. It has already been remarked that the simple gradient law is untenable as a model of the Reynolds stress. Now it will be shown that the properties of displacement transport discussed previously suggest a natural representation of displacement transport in terms of the global properties of the mean velocity gradient. This result is consistent with general observations which have been made concerning the non-local dependence of Reynolds stress on the mean velocity field (Lumley 1983).

A model of the correlation $v_a(\overline{U}_b - \overline{U}_a)$ may be developed from the probability of particle displacement previously considered. Thus, at a particular point y , fluid particles have the probability, say $p_y(r)\Delta r$, of arriving at point y from the neighbourhood $|r - y| < \frac{1}{2}\Delta r$ during the mixing time $\tau^*(y)$. For each of these particles, $\overline{U}_b - \overline{U}_a \approx \overline{U}(r) - \overline{U}(y)$. In addition, these particles travel the distance $r - y$ in the time $\tau^*(y)$ so that it is natural to suggest that on average $v_a \sim -(r - y)/\tau^*(y)$. Introducing a factor $\alpha_y(r)$ it may be asserted that

$$v_a = -\frac{(r-y)\alpha_y(r)}{\tau^*(y)}.$$

In this case the contribution to $\overline{v_a(\overline{U}_b - \overline{U}_a)}$ from particles travelling from a near neighbourhood Δr of r to y in time $\tau^*(y)$ is given approximately by

$$-\frac{(r-y)}{\tau^*(y)}(\overline{U}(r) - \overline{U}(y))\alpha_y(r)p_y(r)\Delta r.$$

Summing this over all r -positions gives the result

$$\overline{v_a(\bar{U}_b - \bar{U}_a)}(y) = -\frac{1}{\tau^*(y)} \int_0^h (r-y)(\bar{U}(r) - \bar{U}(y)) \alpha_y(r) p_y(r) dr. \quad (8)$$

In view of the fact that $\bar{v}_a = 0$ in channel flow, it must be the case that

$$\int_0^h (r-y) \alpha_y(r) p_y(r) dr \equiv 0 \quad (9)$$

if the current model is to be self-consistent. This equation serves as a constraint on $\alpha_y(r)$. If $\alpha_y(r) = 1$, then (9) is equivalent to the statement that the first moment of $p_y(r)$ is zero. However, none of the curves in figure 4 have this property since, as mentioned previously, there is a mean drift of the particles towards the wall. It follows that $\alpha_y(r) \neq 1$, and to balance the asymmetry of $p_y(r)$ it is likely that $\alpha_y(r) < 1$ for $r > y$.

To develop a one-point approximation to the Reynolds stress from (8) one can substitute for $\bar{U}(r) - \bar{U}(y)$ the first N terms in its Taylor series expansion about y . This yields

$$\overline{v_a(\bar{U}_b - \bar{U}_a)}(y) = -\frac{1}{\tau^*(y)} \sum_{n=1}^N \frac{\sigma_{n+1}(y)}{n!} \frac{d^n \bar{U}}{dy^n}(y), \quad (10)$$

where

$$\sigma_n(y) \equiv \int_0^h (r-y)^n \alpha_y(r) p_y(r) dr.$$

When $N = 1$ this simplifies to a gradient transport law in which ν_T in (6) is approximated by $\sigma_2(y)/\tau^*(y)$. The previous results make it quite clear that this degree of approximation is not acceptable. In addition, the large support of $p_y(r)$ evidenced in figure 4 suggests that N must be relatively large if (10) is to capture the non-gradient contribution. Test calculations of the first five terms have been done using the particle path data, which showed that (10) could not be safely truncated at this level. This suggests that it is not possible to develop a practical one-point formula for approximating the Reynolds stress.

An instructive step that may be taken in simplifying (8), which also preserves its global character, is to incorporate into it the identity

$$\bar{U}(r) - \bar{U}(y) = \int_y^r \frac{d\bar{U}}{dy}(s) ds. \quad (11)$$

After reversing the order of integration it follows that

$$\overline{v_a(\bar{U}_b - \bar{U}_a)}(y) = -\frac{1}{\tau^*(y)} \int_0^h \frac{d\bar{U}}{dy}(r) F_y(r) dr, \quad (12)$$

where

$$F_y(r) \equiv \begin{cases} \int_0^r (y-s) \alpha_y(s) p_y(s) ds, & 0 \leq r \leq y, \\ \int_r^h (s-y) \alpha_y(s) p_y(s) ds, & y \leq r \leq h \end{cases}$$

may be regarded as a function that weights the contribution of the mean velocity gradient to the Reynolds stress in a region around y . Figure 17 contains a plot of $F_y(r)$

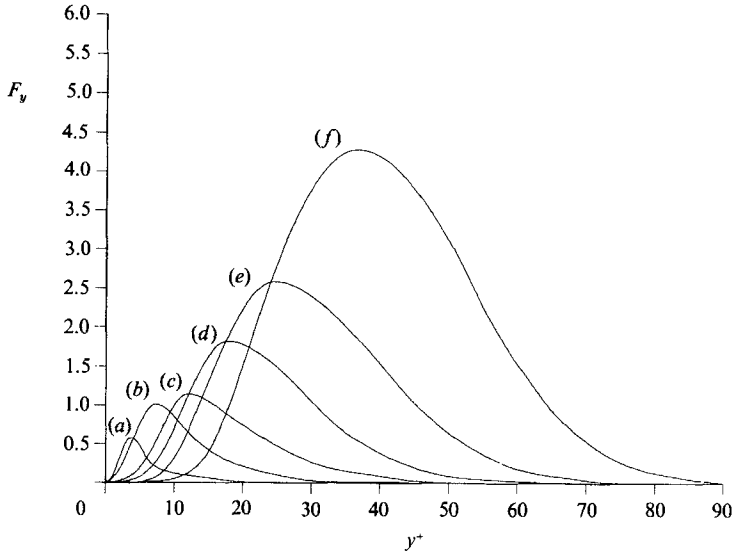


FIGURE 17. The function $F_y(r)$ at each y -position: (a-f) correspond to $y^+ = 3.8, 7.3, 12.0, 17.8, 24.6$ and 36.6 , respectively.

for each of the six y -levels, computed by assuming that $\alpha_y(r)$ is unity for $r < y$ and equal to a constant less than one for $r > y$. The value of the constant is chosen so as to ensure that (9) is satisfied. The computed values of $F_y(r)$ graphically illustrate that the local Reynolds stress depends on flow conditions over a wide spatial range.

Beyond the use that (12) has in concretely expressing the physics of displacement transport, it also has potential benefit in pointing the way towards a practical closure scheme for the Reynolds stress. Clearly, a number of important issues still need to be resolved before the latter goal can be achieved. In particular, it is necessary to better understand the parameters affecting the function $F_y(r)$ so that its form in general flows could be predicted. It also must be recognized that it is necessary to account for the contributions of acceleration transport to the Reynolds stress. These important issues may be treatable by closely examining how vortical elements in the turbulent boundary layer specifically affect the movements of fluid particles.

10. Conclusions

The Reynolds stress has been shown to have its origin in fundamental processes involving the displacement and acceleration of fluid particles. The former, which is the more significant process of the two, arises from the tendency of momentum to be transported unchanged from one level to another by the random motion of fluid elements. Generally, displacement transport is the result of relatively small numbers of particles travelling long vertical distances in the mixing time. These paths appear to be a manifestation of the burst and sweep events usually associated with the dynamics of vortical structures in the wall region. Owing to the inappropriateness of a linear approximation to the mean velocity field over the range travelled by fluid particles during the mixing time, displacement transport was found to be poorly represented by a gradient law. However, as a consequence of its definition, the displacement transport mechanism was shown in (12) to have a natural rep-

resentation in terms of the global distribution of the mean velocity gradient. This result may be of some advantage in the design of improved Reynolds stress models.

The physical process which has been labelled acceleration transport is a consequence of two basic phenomena associated with the change in streamwise velocity of fluid particles. Near the wall this primarily consists of the deceleration of fluid particles contained in sweep events by the action of viscous and pressure forces. This process acts to reduce the total Reynolds stress. Further from the wall Reynolds stress is generated when fluid particles decelerate while spiralling towards and then away from the wall. In addition, the inverse process may occur in which particles accelerate while heading away from and then towards the wall. For these motions the net vertical displacement of the fluid particles is relatively small.

The fluid particle motions most closely connected to the displacement transport mechanism appear to be largely distinct from those occurring in acceleration transport. An important exception is the decelerating sweep events near the wall which contribute significantly to both modes of transport. In spite of the differences between the two sets of paths, a common ground between them may lie in the fact that they appear to represent different aspects of the motions associated with vortical structures in the turbulent boundary layer. This connection with the structural aspects of turbulent flow will be pursued further using three-dimensional animated visualizations of the fluid particle paths. An understanding of the particular effects of vortices on particle motions may suggest a means for bringing formula (12) to a practical level and for modelling the acceleration transport contribution to Reynolds stress.

The Lagrangian approach pursued here may be applied to the analysis of a broad range of physical processes in turbulent flow. In future work concerned with momentum transport, it is intended to study the relative contributions that pressure and viscous forces make to acceleration transport and to investigate the nature of the Reynolds stress in the central region of the channel. It is also planned to apply similar analyses to studies of vorticity transport and scalar diffusion.

The assistance of Dr Richard Leighton in the development of the direct numerical simulation code is greatly appreciated. Support of P. S. Bernard for this study was provided in part through an ASEE/Navy Summer Faculty Research Fellowship at the Naval Research Laboratory, Washington, DC.

REFERENCES

- AZAB, K. A. & McLAUGHLIN, J. B. 1987 Modeling the viscous wall region. *Phys. Fluids* **30**, 2362–2373.
- BERNARD, P. S., ASHMAWEY, M. F. & HANDLER, R. A. 1989*a* Evaluation of the gradient model of turbulent transport through direct Lagrangian simulation. *ALAA J.* **27**, 1290–1292.
- BERNARD, P. S., ASHMAWEY, M. F. & HANDLER, R. A. 1989*b* An analysis of particle trajectories in computer simulated turbulent channel flow. *Phys. Fluids A* **1**, 1532–1540.
- BRODKEY, R. S., WALLACE, J. M. & ECKELMANN, H. 1974 Some properties of truncated turbulence signals in bounded shear flows. *J. Fluid Mech.* **63**, 209–224.
- CORRSIN, S. 1974 Limitations of gradient transport models in random walks and turbulence. *Adv. Geophys.* **18A**, 25–60.
- DEARDORFF, J. W. & PESKIN, R. L. 1970 Lagrangian statistics from numerically integrated turbulent shear flow. *Phys. Fluids* **13**, 584–595.
- HANDLER, R. A., HENDRICKS, E. W. & LEIGHTON, R. I. 1989 Low Reynolds number calculation of turbulent channel flow: a general discussion. *Naval Research Laboratory Mem. Rep.* 6410.

- HINZE, J. O. 1975 *Turbulence*, 2nd edn. McGraw-Hill.
- KIM, J., MOIN, P. & MOSER, R. 1987 Turbulence statistics in fully developed channel flow at low Reynolds number. *J. Fluid Mech.* **177**, 133–166.
- LAKSHMINARAYANA, B. 1986 Turbulence modeling for complex shear flows. *AIAA J.* **24**, 1900–1917.
- LUMLEY, J. 1983 Turbulence modeling. *J. Appl. Mech.* **50**, 1097–1103.
- MARCUS, P. S. 1984 Simulation of Taylor–Couette flow. Part 1. Numerical methods and comparison with experiment. *J. Fluid Mech.* **146**, 45–64.
- ORSZAG, S. A. & KELLS, L. C. 1980 Transition to turbulence in plane Poiseuille and plane Couette flow. *J. Fluid Mech.* **96**, 159–205.
- PESKIN, R. L. 1974 Numerical simulation of Lagrangian turbulent quantities in two and three dimensions. *Adv. Geophys.* **18A**, 141–163.
- PIOMELLI, U., MOIN, P. & FERZIGER, J. 1989 Large eddy simulation of the flow in a transpired channel. *AIAA paper* 89-0375.
- PRANDTL, L. 1925 Über die ausgebildete Turbulenz. *Z. Angew. Math. Mech.* **5**, 136–138.
- ROBINSON, S., KLINE, S. J. & SPALART, P. R. 1988 Quasi-coherent structures in the turbulent boundary layer. *Proc. Zoric Memorial Intl Sem. on Near-Wall Turbulence, Dubrovnik, Yugoslavia*. Hemisphere.
- SPEZIALE, C. G. 1987 On nonlinear $K-l$ and $K-\epsilon$ models of turbulence. *J. Fluid Mech.* **178**, 459–475.
- TAYLOR, G. I. 1915 Eddy motion in the atmosphere. *Phil. Trans. R. Soc. Lond.* **215**, 1–26.
- TAYLOR, G. I. 1932 The transport of vorticity and heat through fluids in turbulent motion. *Proc. R. Soc. Lond. A* **135**, 685–705.
- TENNEKES, H. & LUMLEY, J. L. 1972 *A First Course in Turbulence*. MIT Press.
- WALLACE, J. M. 1985 The vortical structure of bounded turbulent shear flow. In *Flow of Real Fluids*. Lecture Notes in Physics, vol. 235, pp. 253–268. Springer.
- YEUNG, P. K. & POPE, S. B. 1988 An algorithm for tracking fluid particles in numerical simulations of homogeneous turbulence. *J. Comput. Phys.* **79**, 373–416.